THE JOURNAL OF PHYSICAL CHEMISTRY C
A JOURNAL OF THE AMERICAN CHEMICAL SOCIETY

pubs.acs.org/JPCC

Article

Atomically Smooth Fully Hydroxylated CeO_2(001) Films on YSZ(001)

Jan-Christian Schober,* E. Erik Beck, Ming-Chao Kao, Mona Kohantorabi, Marcus Creutzburg, Dmitri V. Novikov, Thomas F. Keller, Birger Holtermann, Nadejda Firman, Lachlan Caulfield, Eric Sauter, Vedran Vonk, Christof Wöll, Yuemin Wang, Heshmat Noei, Yolita M. Eggeler, and Andreas Stierle*

Cite This: J. Phys. Chem. C 2024, 128, 19795−19806

Read Online

ACCESS | Metrics & More | Article Recommendations | Supporting Information

ABSTRACT: CeO_2 is an important support material with redox properties interesting for heterogeneous catalysis and energy conversion applications. Here, we present a facile growth procedure for epitaxial CeO_2(001) thin films supported by YSZ(001) suitable for combined catalytic activity and structural investigations. The growth of the CeO_2 thin films was performed using standard ultrahigh-vacuum (UHV) preparation techniques followed by tube furnace annealing in air. Thorough characterization prior to and after the tube furnace annealing revealed that this step induces significant restructuring of the film. Complete characterization by atomic force microscopy (AFM), X-ray reflectivity (XRR), grazing incidence X-ray diffraction (GIXRD), cross-section high-resolution scanning tunneling electron microscopy (HR-STEM), X-ray photoemission spectroscopy (XPS), and polarization-resolved infrared reflection absorption spectroscopy (IRRAS) showed that the film is fully oxidized and atomically smooth with a coherent crystal lattice over the full film thickness. A dislocation network at the CeO_2/YSZ interface compensates the lattice mismatch between film and the YSZ support, yielding a film with bulk lattice parameters. The bulk terminated surface is found to be defect free with negligible amount of adsorption sites and stabilized by the presence of hydroxyl groups for polarity compensation.

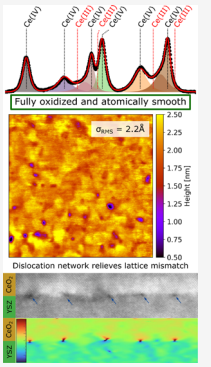

INTRODUCTION

Ceria is a complex oxide material with rich structural, chemical and catalytic properties.[1−4] Central to many applications is the fast incorporation (release) of oxygen into (from) the lattice. This is possible due to the facile and reversible change in oxidation state from Ce(IV) to Ce(III) without significant changes to the crystal structure. Prominent examples for such applications are solid oxide fuel cells (SOFC), gas sensors, and the use of ceria in heterogeneous catalysis as support or catalyst.[5−8] A large number of reports on structure, chemistry and catalytic activity[1−4,6−17] highlight the need for detailed structural and chemical control of CeO_2 model surfaces, which also permits a direct comparison with theoretical results.

Several studies in the last decades were directed toward understanding the growth and structure of CeO_2 thin films on various oxide and metal substrates.[3,−22] However, most studies only focused on single aspects of the films such as interface structure, growth mechanisms or structural and compositional changes in oxidizing (reducing) environments. For structurally well-defined ultrathin CeO_2 thin films, Ru or Pt are common supports,[18,19,23−25] however, catalytically active support crystals are inconvenient for operando catalytic studies. Films grown on inert oxides such as MgO, Al_2O_3, Pr_2O_3, or YSZ (Y stabilized ZrO_2) are frequently manufactured by pulsed laser deposition (PLD), atomic layer deposition (ALD), or molecular beam epitaxy (MBE) with varying structural and chemical control.[1,20,21,26,27] High structural and chemical control over the CeO_2 thin film can be achieved e.g., by using Pr_2O_3(0001) buffer layer between the CeO_2 thin film and a Si(111) substrate. However, sample preparation involves hazardous materials and multiple growth steps with the need to remove and reintroduce the sample from and to UHV.[28] Reports on the interface structure between CeO_2 thin films and YSZ single crystal substrates showed that the lattice mismatch between the two materials is relieved by dislocations,[1,27] but no information on the surface structure or chemistry is provided. Theoretical studies and experiments on the surface of CeO_2(111) showed the formation of surface and subsurface oxygen vacancies[29] which are crucial for the redox properties of CeO_2 and were linked to improved catalytic activity[30] and increased stabilization of adsorbed OH species.[31,32]

In other studies CeO_2 single crystals and their behavior upon reducing or oxidizing treatments were investigated.[20,33] Some studies report the observation of well-defined vibrations of adsorbed CO on CeO_2 single crystal surfaces distinctly different for different surface orientations revealed the presence

Received: July 3, 2024
Revised: October 21, 2024
Accepted: October 22, 2024
Published: November 6, 2024

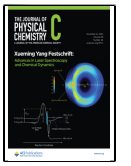

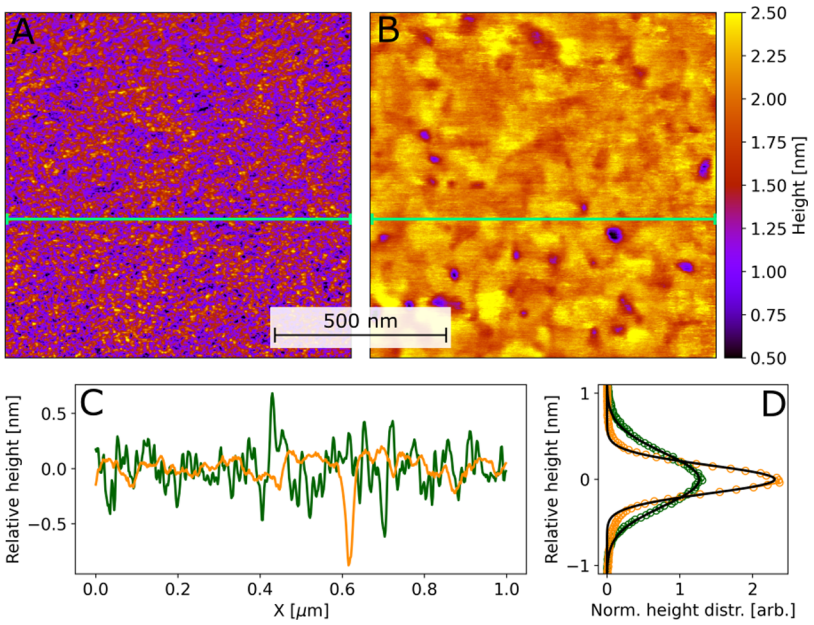

Figure 1. AFM images with identical height color map and lateral scale recorded before (A) and after (B) annealing in air for comparison. (C) line scans (green: before tube furnace annealing in air, orange: after tube furnace annealing in air) indicated by the green, horizontal lines in (A, B) are shown. (D) relative height as a function of the height distribution (green: before tube furnace annealing in air, orange: after tube furnace annealing in air). For both distributions the fitted Gaussian profiles are plotted in black.

of rather homogeneous surfaces.[34−37] In other cases poor surface quality was observed, as visualized in the scanning micrograph of a freshly polished CeO_2(111) single crystal in Figure S1. Furthermore, in other studies CeO_2 single crystals were reported to contain significant fluorine contaminations leading to an altered surface chemistry.[38,39]

Here, we present a facile, straightforward growth procedure for fully oxidized CeO_2(001) thin films with atomically smooth surfaces on YSZ(001). The resulting films were prepared using standard UHV techniques which can be easily reproduced. We thoroughly characterized the films' bulk and interface structure to the substrate using grazing incidence X-ray diffraction (GIXRD), X-ray reflectivity (XRR), and high-resolution scanning tunneling electron microscopy (HR-STEM). Further information on the surface structure of the films was obtained by atomic force microscopy (AFM), and crystal truncation rod (CTR) analysis, while X-ray photoemission spectroscopy (XPS) and polarization-resolved infrared reflection absorption spectroscopy (IRRAS) were employed in order to understand the chemical state of the film surface. This combination of complementary techniques draws a complete picture of the chemical, structural, and morphological features of the films' bulk and surface properties.

METHODS

AFM data was recorded in air using tapping mode and oxide-sharpened silicon cantilevers with a nominal tip radius of 8 nm and a resonance frequency of 300 kHz.[40] For all measurements a scanning speed of 0.5 Hz was used. To consider potential sample tilts from mounting, a polynomial plane fit was applied.

CTR data was recorded at the P23 beamline of PETRA III at an X-ray energy of 16 keV using a 5 + 2 circle diffractometer under grazing incidence with a GaAs 2D LAMBDA pixel detector. Throughout the measurement the sample was under 100 mL/min Ar flow at a constant pressure of 100 mbar. All XRR and GIXRD data, except for the CTR data, were recorded at the DESY Nanolab[40] 6-circle diffractometer using Cu Kα radiation, a parabolic multilayer optics for focusing, and a Lambda 750 K detector.

The X-ray photoemission spectroscopy (XPS) measurements were conducted at DESY NanoLab[40] using a monochromatic Al Kα source ($h\nu$ = 1486.6 eV) and a hemispherical energy analyzer. A flood gun was used during the measurements at an energy 2.0 eV with 20 μA emission for charge compensation. Ce 3d core level spectra were recorded using a pass energy of 30 eV and a step size of 0.1 eV, the survey scan from 0 to 1200 eV recorded at normal emission in Figure S9 was performed with a pass energy of 50 eV and a step size of 0.5 eV.

The polarization-dependent IRRAS experiments were conducted with an UHV apparatus combining a state-of-the-art FTIR spectrometer and a multichambered UHV system. This dedicated apparatus was built in a way that the spectrometer can be attached to the experimental chamber and guides the IR light trough the UHV chamber. Additionally, it allows performing UHV preparation as well as IR experiments on samples without exposure to atmosphere.

The crystal was placed on a sample holder specifically designed for IRRAS measurements. After introduction of the crystal into UHV (10^{-10} mbar) the CO adsorption experiments were performed for the pristine and cleaned surface. The surface was cleaned at 550 °C, for 30 min, in the presence of oxygen (O_2, 1×10^{-4} mbar) to get the fully oxidized, cleaned surface. After cooling the sample to temperatures as low as 65 K, exposure to carbon monoxide (CO) was achieved using a leak-valve-based directional doser connected to a tube of 2 mm in diameter, which is terminated 30 mm from the sample surface and 50 cm from the hot-cathode ionization gauge. The polarization-resolved IRRAS spectra were recorded with both s- and p-polarized light at a fixed grazing incidence of 80°. All IRRAS data shown here are difference spectra obtained by subtracting the reference. The IR spectra were

https://doi.org/10.1021/acs.jpcc.4c04438
J. Phys. Chem. C 2024, 128, 19795−19806

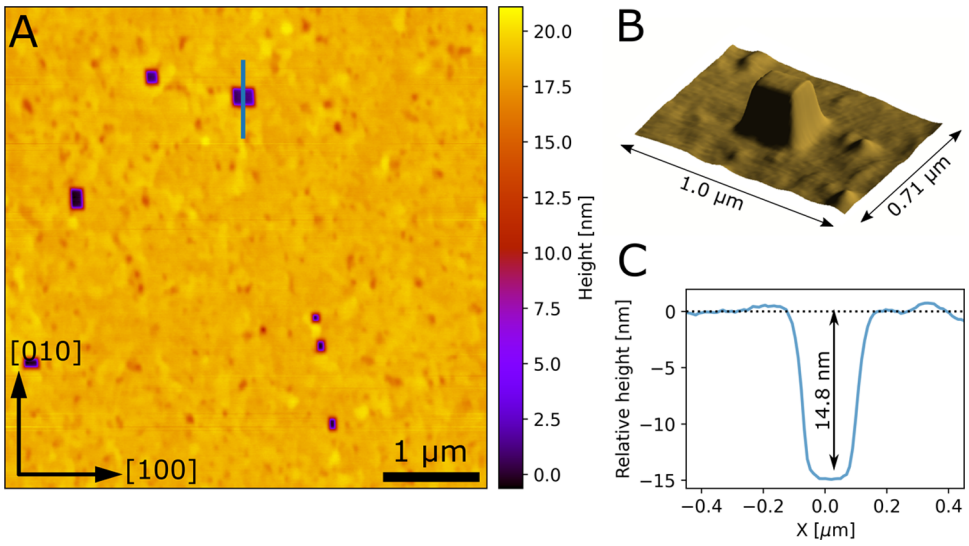

Figure 2. (A) AFM image of an area of the film after annealing exhibiting holes. (B) Inverted 3D view of one hole. (C) Line scan through the hole.

acquired by recording 1024 scans with a resolution of 4 cm^{-1}. Exposures are given in units of Langmuir (L) (1 L = 1.33 × 10^{-6} mbar s).

For the preparation of the HR-STEM specimen, the sample was first coated with 30 nm amorphous carbon in a sputter coater and then a dual focused ion beam instrument was used to cover the selected region of interest with an amorphous protective Pt cover before milling a TEM lamella.

RESULTS AND DISCUSSION

For CeO_2 growth, the YSZ(001) substrate single crystals with a miscut of <0.1° and 9% Y_2O_3 were used. After introduction into UHV (base pressure <1 × 10^{-10} mbar), the substrates were heated to 600 °C with a ramp of 15 °C/min using electron beam (e-beam) heating. After degassing at 600 °C for 30 min, the substrate was further annealed for 120 min at this temperature in 5 × 10^{-6} mbar oxygen (99.995% purity) to ensure a fully oxidized surface. To confirm the cleaning procedure, the Auger electron spectroscopy (AES) data shown in Figure S2 reveals only negligible signal of carbon contamination (~273 eV), but strong Y and O signal. After heating the sample to the deposition temperature of 400 °C, the CeO_2 films were grown by reactive deposition at a rate of ~1.2 Å/min. Ce metal with a purity of 99.9% was evaporated from a crucible using an e-beam evaporator in an oxygen background pressure of 5 × 10^{-6} mbar, supplied through an oxygen thermal cracker providing ~10% atomic oxygen. The atomic oxygen back pressure was maintained until the sample reached room temperature. Due to severe charging of the sample after the deposition, AES and low energy electron diffraction characterization could not be performed to further investigate the film before removing from UHV. Further improvement of the films' structural properties was achieved by annealing them in air in a tube furnace. The annealing procedure consisted of a single annealing step at 1100 °C for 260 min (cooling/heating ramps of 1200 °C/h).

Surface Morphology of the CeO_2 Films. The atomic force microscopy (AFM) height images in Figure 1 show the film before (A) and after (B) annealing with the as-prepared CeO_2 film likely consisting of closely packed, small crystallites fully covering the surface. For both images, line profiles with a width of 5.12 nm, corresponding to 10 pixels (Figure 1(C)), height distribution profiles (Figure 1(D)) showing the frequency of a given height around the mean height, and the root-mean-square (RMS) roughness were calculated using Gwyddion.[41] The line profiles illustrate the improvement in surface smoothness best. Before the tube furnace annealing, the surface has a peak-to-valley distance of ~1.2 nm. Disregarding the small hole at x = 0.6 μm, the line profile of the sample after annealing (orange) is significantly smoother, with a peak to valley distance of 0.42 nm. The corresponding height distribution profiles reflect this as well. The fwhm of the height distribution profiles with a unimodal Gaussian shape decreases by ~50% from 0.74 ± 0.002 nm before the tube furnace annealing to 0.39 ± 0.002 nm afterward (see Table S1 and accompanying text for fit parameters). The smoothness of the CeO_2 film after the tube furnace annealing is also apparent from the AFM image in Figure 1(B) with much larger areas of similar height. The RMS roughness $\sigma = \sqrt{\frac{1}{N}\sum_{n=1}^{N}(z_n - \overline{z})^2}$, where N is the number of height values, z_n the nth height value and $\overline{z}$ the average height), was calculated from the images in Figure 1(A,B) and improved from 0.33 to 0.22 nm after annealing.[41]

The large overview image in Figure S3 that also contains the area of Figure 1 reveals that the CeO_2 film is interrupted by rectangular holes. Up to this point an area without holes was chosen to gain information on the film surface morphology without distorting statistics by the holes interrupting the film. In order to investigate the holes in detail, we performed AFM measurements on another sample with the crystal principle [100] and [010] axes aligned with the x, y image axes, as shown in Figure 2(A). In Figure 2(B), a three-dimensional (3D) rendering with inverted z-axis is shown, highlighting the hole's uniform, rectangular shape, indicating ⟨100⟩-type side facets. Figure 2(C) shows a line scan of the hole at the position marked by the line with corresponding color in Figure 2(A). The depth of the hole is in good agreement with the film thickness of 14.4 nm determined by XRD (see Figure S4 and Table S2, and accompanying text), indicating that they reach down to the surface of the YSZ substrate. A possible origin of the holes will be discussed further below.

Structural Properties of CeO_2 Films. XRR measurements were employed to gain information on film thickness,

https://doi.org/10.1021/acs.jpcc.4c04438
J. Phys. Chem. C 2024, 128, 19795−19806

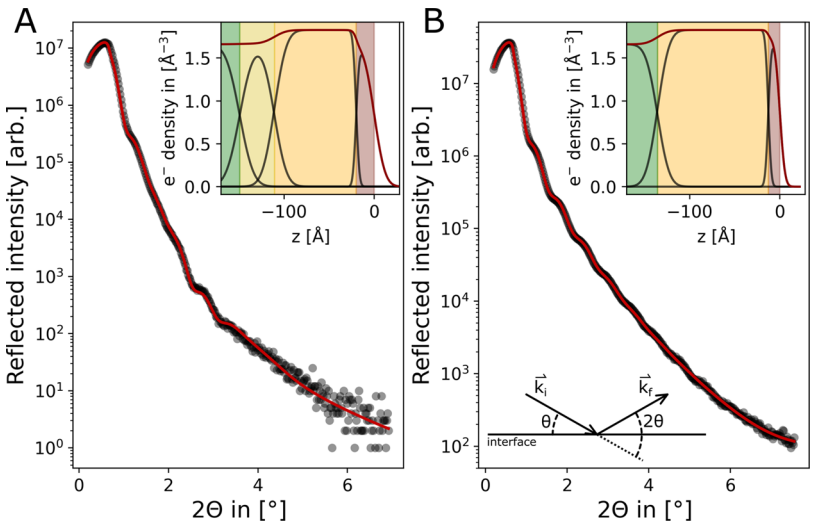

Figure 3. Specular reflected intensities as a function of the reflection angle 2Θ (black dots), with fitted curve (red, solid line). Inset: Electron density profile of fitted model (red line) with the components (black lines), before and after furnace anneal (A, B). Yellow, orange and red rectangles indicate CeO_2 layers, the green rectangle the YSZ substrate.

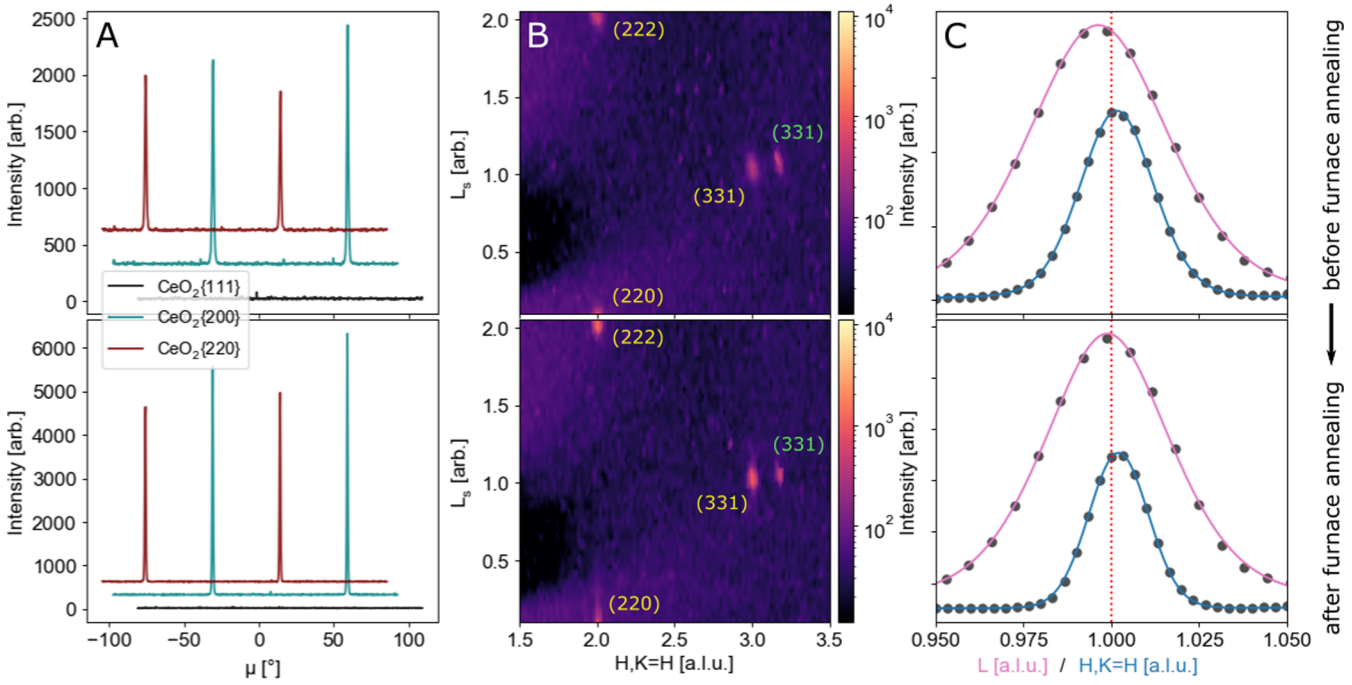

Figure 4. (A) Rocking scans of the sample rotation μ, corrected for the in-plane Bragg angle, showing 45° spacing between in-plane (200)- and (220)-like reflections and absence of (111)-type reflections. (B) Reciprocal space maps revealing $CeO_2(001)$/YSZ(001) cube-on-cube epitaxy without any other phases or orientations. CeO_2 reflections labeled in orange, YSZ reflections in green. (C) Line scans through the $CeO_2(111)$ Bragg peak along $H,K = H$ (radial) and L direction (blue and pink, respectively). For all images (A–C), the top image was recorded before, the bottom image after tube furnace annealing.

coverage, and interfacial roughness, complementary to the AFM investigations. All XRR data was fitted using the Parratt formalism[42,43] and fit results of the material parameters are given in Table S3. To fit the data recorded before tube furnace annealing, shown in Figure 3(A), a three-layer model was chosen to accommodate three distinct features of the film: A depletion region (yellow) with reduced electron density compared to YSZ and CeO_2 at the interface to the substrate, the bulk of the film with CeO_2 bulk electron density (orange), and a top-layer with a reduced electron density (red) accommodating the rough morphology of the as-prepared film. In agreement with the height distribution profiles in Figure 1(D), a Gaussian roughness model was used to smoothen the transitions between the layers. The total film thickness, as determined from XRR, is 14.9 nm. The central layer, representing the majority volume of the film, possesses the bulk electron density of CeO_2, which allows to conclude that the YSZ substrate is fully covered by the CeO_2 film, confirming the AFM observations in Figure 1(A) where no interruption of the film was observed. The terminating layer of the CeO_2 film has a thickness of 2.0 nm with a surface RMS roughness of 0.95 nm, which exceeds the RMS roughness

https://doi.org/10.1021/acs.jpcc.4c04438
J. Phys. Chem. C 2024, 128, 19795−19806

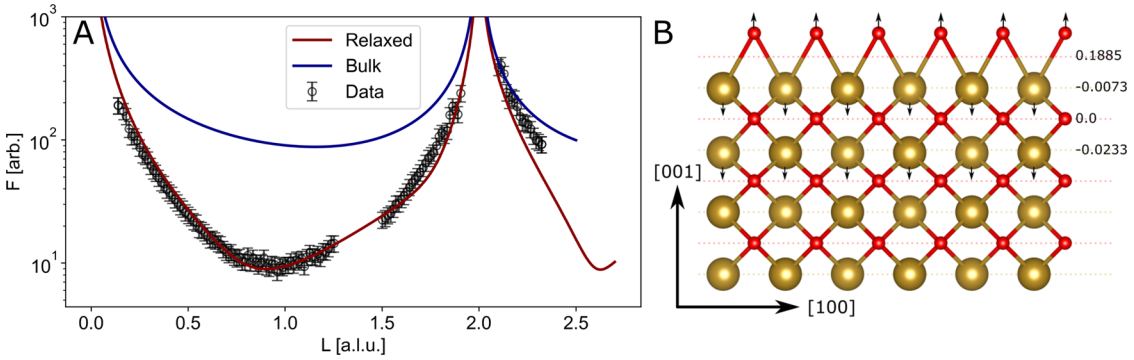

Figure 5. (A) (22L) rod of CeO_2(001) thin film (black circles and error bars) with CTR model of the bulk truncated model (blue) and the CTR model including relaxation of the surface layer along z (red). (B) Model of the relaxed surface structure of the (001)CeO_2 film. The dotted lines indicate the original positions of the layers, the small black arrows the direction of the displacement.

calculated from the AFM image by a factor of nearly three. The reason for this discrepancy can be of experimental and physical origin. Experimentally, the limited resolution due to convolution of the AFM tip with surface shape and inaccuracies in model choice can lead to smaller RMS roughness values in AFM and larger values in XRR analysis. However, since the roughness model fits well with the height distribution profile and the aforementioned errors cannot account for such a large difference, the top layer of the XRR model is not only reproducing morphological roughness but likely reduced density due to vacancies, loosely packed crystallites, and amorphous CeO_2.

A first, qualitative comparison of the XRR data obtained before and after the furnace annealing (Figure 3(A,B)), confirms the observations in the AFM measurements. The most significant changes in the XRR curve after annealing (Figure 3(B)) are the lack of modulation in the oscillations at $1.5° < 2\Theta < 2.5°$ and an overall intensity increase due to reduced roughness and possibly elimination of nonreflective areas. Overall, the electron density of the film is that of bulk CeO_2 before as well as after the tube furnace annealing, which previously could not be observed in doped films grown by PLD.[44] This is the case despite the rectangular holes observed in AFM, indicating the holes are sparse, local features that do not contribute significantly to the average film electron density. The model could be simplified by the removal of the low density interfacial layer. It apparently restructured during the tube furnace annealing leading to the sharper substrate−film interface in the electron density profile in Figure 3(B). The surface roughness of the top layer is 0.44 nm, less than half compared to before annealing (0.95 nm) and matches the AFM RMS roughness of 0.58 nm observed for the overview image, including the holes in Figure S3. As apparent from the comparison of the electron density profiles depicted in Figure 3(A,B), the top CeO_2 layer of the model reduced significantly in width from 2.0 to 1.3 nm and in electron density. This leads to a far more abrupt cutoff of the total electron density, signifying a strongly reduced surface roughness. In addition, the total film thickness is reduced from a value of 14.9 to 13.6 nm, while the thickness of the bulk CeO_2 layer increased from 9.07 ± 0.18 to 12.28 ± 0.07 nm. We explain these changes in the film density, thickness, and roughness at both interfaces by a significant restructuring process that involves optimization of the interface structure between the YSZ substrate and the CeO_2 thin film as well as oxidation of the film at the interface.

Next we will discuss the structural properties of the CeO_2 film. In Figure 4(A), rocking scans with the rotation axis along the surface normal are shown. For this, the detector position was fixed at the respective in-plane Bragg angles for (111), (200), and (220) reflections of CeO_2. These scans allow us to determine the film epitaxy and its preferential growth directions. In Figure 4(A−C), the top panel contains data recorded before the tube furnace annealing, while the bottom panel displays data obtained after. Since only the (200) and (220) rocking scans show diffraction signal and both scans have 4-fold symmetry with a 45° spacing between them, the film is exclusively (001) oriented. The reciprocal space maps in Figure 4(B) reveal YSZ and CeO_2 (331)-type reflections in the $H, K = H, L$ plane indicating that the film conforms to cube-on-cube epitaxy. No additional phases, such as Ce_2O_3, or metallic Ce or other orientations of CeO_2 were observed neither before, nor after tube furnace annealing. However, the peak intensity in the rocking scans increased by a factor of 2 while the peak width decreased in both radial and azimuthal directions (Figure 4(A)). The latter indicates a change in coherent crystallite size, which was determined by line scans through the CeO_2(111) Bragg peak along the L direction (height) and $H,K = H$ (radial) direction (lateral size), as presented in Figure 4(C). Based on the fitted fwhm the coherent crystallite size D can be calculated along the respective direction using $\Delta Q = \frac{2\pi}{D}$.[45] Before the tube furnace annealing, the lateral coherent crystallite size is determined to be 25.3 nm and the coherent height is 12.9 nm. The large difference to the total film thickness of 15 nm determined by XRR, can be explained by structural heterogeneity: The film consists of CeO_2 crystallites, giving rise to the characteristic diffraction signal, as well as amorphous, (partially reduced) CeO_2 only contributing to the XRR height. After the tube furnace annealing, the coherent crystallite size grows to 14.3 nm perpendicular to the surface and laterally by roughly 25%, to 31.6 nm. In the XRR measurement the opposite behavior, a decrease in the total film thickness, is observed, allowing the conclusion that amorphous parts of the film crystallize. In fact, the coherent crystal size with 14.3 nm is slightly larger than the observed thickness from XRR of 13.6 nm, but agrees within the error bars of measurements and fits. We quantified the reduction in mosaicity by the average fwhm of the in-plane (200)- and (220) rocking scans (Figure 4A). For the as-prepared film the fits (see Figure S5 for fits and Table S6 for fit parameters) yielded a mosaicity distribution of 1.23° for the (200) type reflection, while after the tube furnace annealing

https://doi.org/10.1021/acs.jpcc.4c04438
J. Phys. Chem. C 2024, 128, 19795−19806

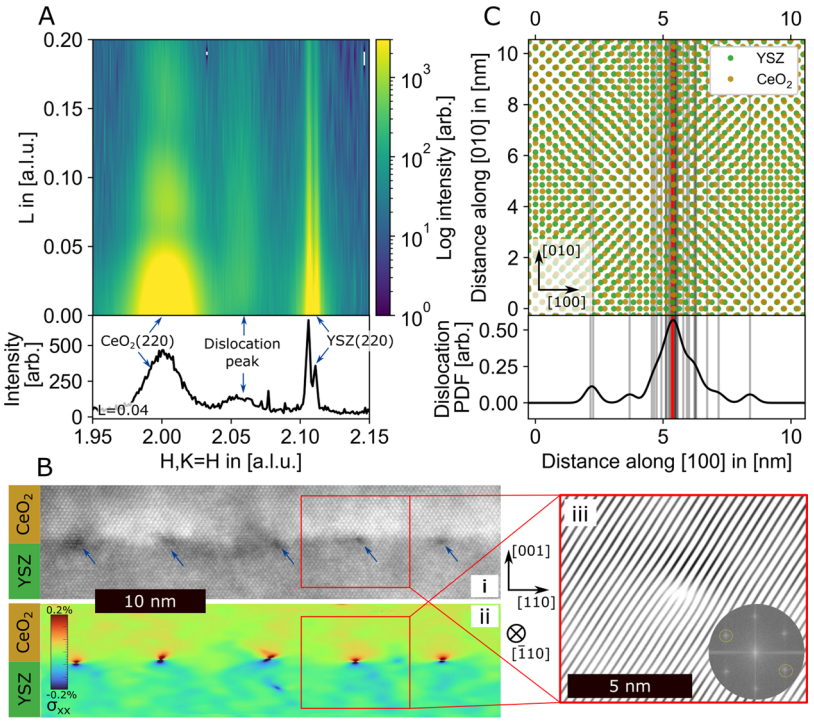

Figure 6. (A) Reciprocal space map (top) and line scan (bottom) in the vicinity of the CeO_2 and YSZ (220) reflections. (B)(i): HR-STEM image of the CeO_2 film (top) and YSZ substrate (bottom), projecting the [110] and [001] directions in the plane of the image. (B)(ii): σ_{xx} component of the strain tensor from geometric phase analysis of the area in (B)(i). (B)(iii): ±(111) Bragg filtered image corresponding to the red rectangle in (B)(i). Crystal axes for all HR-STEM data are indicated next to the (B) (iii). (C) Calculated coincidence lattice for CeO_2 (yellow) and YSZ (green). The points indicate atomic positions of metal ions in 001-type planes (i.e., the faces of the fcc unit cell) and nicely demonstrates the deviation from a perfect coincidence lattice and hence the location of a necessary misfit dislocation.

the fwhm reduced by more than one-third to 0.80°. Similar values were attained for the (220) type reflection indicating, together with the increase in coherent crystallite size, a significant restructuring process during the tube furnace annealing to larger, well aligned domains.

From the peak positions in Figure 4(C), the lattice parameters along the respective scan directions were calculated. The peak positions expected from the bulk lattice constant are indicated by the red, dotted lines. In-plane (H, $K = H$), the lattice constant increases from 5.408 ± 0.008 Å before to 5.418 ± 0.008 Å (bulk lattice constant 5.4178 Å[46]) after the furnace annealing. The out-of-plane lattice constant decreases slightly from 5.46 ± 0.02 to 5.41 ± 0.008 Å before and after annealing, indicating a relaxation of the film toward the bulk lattice constant. The lattice constants were refined using multiple CeO_2 reflections (see Table S5). Within these error bars, lattice parameters of the films are found to be fully relaxed to bulk stoichiometric CeO_2. The lack of uniform strain indicates that the lattice mismatch between YSZ and CeO_2 is likely relieved by dislocations.

Further information on the surface structure of the film was obtained by analysis of surface X-ray diffraction CTR data recorded at the PETRA III beamline P23. In contrast to XRR and AFM that probe the surface morphology, CTR analysis probes the termination of the crystalline lattice of the film.[47] In Figure 5(A), the measured (22L) CeO_2 CTR and the X-ray structure factor of 2 fitted surface models are shown. Since the film surface is much smoother than its interface, a simplified model of only the top surface of the film was used. For the bulk simulation (blue curve in Figure 5(A)), no parameters except a scaling factor was varied. The clear discrepancy between fitted model and data shows that the model is not representing the surface structure well. The adapted surface model includes a roughness parameter β, and relaxations of the atoms from their bulk position along the surface normal. The structural model is shown in Figure 5(B) and includes the relative displacement of the atoms on the right-hand-side. This simulation already yields good agreement between data and fit: The decreased scattered intensity is due to the surface roughness represented by the parameter β. For comparison with other techniques, the RMS roughness of 9.6 Å was calculated using $\sigma_{\mathrm{RMS}}(\beta) = \frac{\beta^{0.5}}{1-\beta} \cdot d_{\perp}$, where β is the fitted roughness parameter and $d_{\perp} = \frac{a_0}{2}$ with a_0 = 5.41 Å is the lattice distance along the surface normal.[48] The value is in reasonable agreement with the values from XRR and AFM, indicating that the film is fully crystalline, as only the crystalline phase contributes to β. The top O and Ce layers are relaxed from the original atomic positions, as indicated by the dotted lines and arrows. The top Ce layer is slightly compressed and the top oxygen layer is significantly expanded along the surface normal. This is in contrast to previous studies on single crystals and nanoparticles where reconstruction and massive restructuring of the (001) termination were reported.[35] We attribute the displacement of the top O layer to hydroxyl groups (see discussion below). Due to the small contribution to the electron density, H atoms were not included in the fit.

Interfacial Dislocation Network. Next we will discuss the misfit relaxation mechanism between the CeO_2 film and YSZ substrate. In Figure 6(A), a reciprocal space map of the [H, $K = H$, L] plane in the vicinity of the in-plane CeO_2 and YSZ (220) reflections is shown. The (22L) crystal truncation rod

https://doi.org/10.1021/acs.jpcc.4c04438
J. Phys. Chem. C 2024, 128, 19795−19806

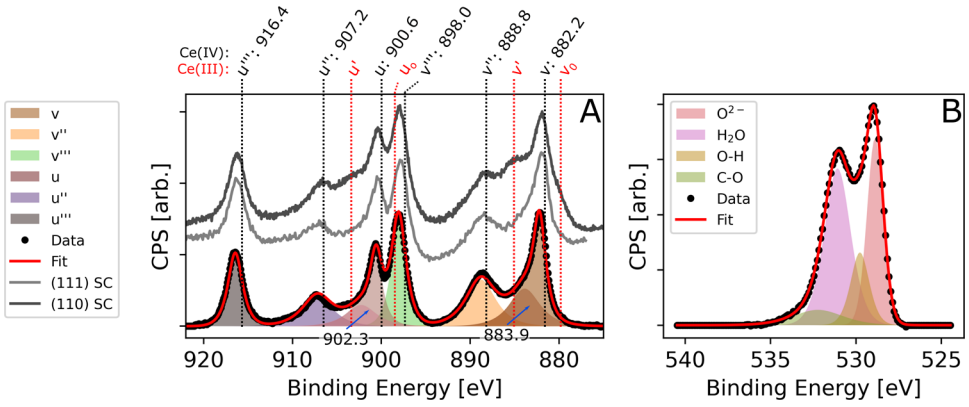

Figure 7. Deconvoluted Ce 3d (A) and O 1s (B) core level spectra of the thin film after tube furnace annealing at 50° emission angle (black dots) including fit (red line) and components (colored areas). For comparison, reference core level spectra of a (111) faceted CeO_2(110) single crystal (data provided by the authors of[54]) and an untreated CeO_2(111) single crystal, recorded at the same emission angle are shown with fitted data in (A). In addition, the fitted peak positions of the Ce(IV) 3d core levels as well as the expected positions of Ce(III) 3d core levels from[55] are shown.

(CTR) signal of CeO_2 exhibits film thickness oscillations, which appear for atomically flat films with macroscopically coherent film thickness. Between the CTRs of CeO_2 and YSZ (split due to contributions of Cu $K_{\alpha,1}$, $K_{\alpha,2}$ radiation in the X-ray beam of the laboratory source), an additional diffraction signal can be observed. It is centered between the film and substrate (220) reflections at H = 2.06 (see line scan at L = 0.04 in the bottom panel of Figure 6(A)). This satellite peak occurs due to an ordered misfit dislocation network, a long-range ordered lattice of dislocations at the interface between CeO_2 and the YSZ substrate.[49] A periodicity of 7.08 ± 0.10 nm was determined from the dislocation peak position,[50] relative to the CeO_2 (220) reflection (see Figure S6 and Table S7 for fits and full set of fit parameters).

Further information on the misfit dislocation network was obtained by HR-STEM measurements shown in Figure 6(B). For these measurements, a cross-section specimen with its normal oriented along the $[\bar{1}10]$ direction was prepared (see Methods section). Figure 6(B) shows (i) the average background subtraction filtered (ABSF) HR-STEM image, (ii) the corresponding σ_{xx} component of the strain tensor calculated by geometric phase analysis (GPA),[51,52] and (iii) a Bragg filtered image isolating one of the misfit dislocations. In the HR-STEM image, the less scattering and hence darker bottom area corresponds to YSZ while the brighter and hence more scattering upper area corresponds to CeO_2, as labeled on the left side. The periodically darker contrast with an average distance of 7.58 ± 1.8 nm at the interface of the two materials, indicated by blue arrows, are attributed to dislocations. The highly localized opposite sided strain fields with opposing signs at those positions in Figure 6(ii) confirm the assignment as dislocations. One of the misfit dislocations was investigated by Bragg filtering which shows the extra half plane at the interface of the isolated CeO_2 111 and YSZ 111 planes in Figure 6(B)(iii).

In the top panel of Figure 6(C), the lattices of 001 planes of CeO_2 (yellow) and YSZ (green) are shown with the circles representing the atomic positions in that plane. The gray lines are the dislocation distances, measured from two Bragg filtered images using different reflection pairs of the three images in Figure S7. The red line is the mean dislocation distance of 7.58 ± 1.8 nm. The lines are extended into the bottom panel of Figure 6(C), where the dislocation probability density function emphasize the unimodal distribution centered around the mean distribution value. All distances and the calculation is given in Table S8 and the accompanying text. The average spacing of the misfit dislocations obtained from the HR-STEM image analysis and the value obtained from GIXRD analysis are slightly smaller than the calculated equilibrium spacing of 7.8 nm for dislocations of Burgers vector type $b = \frac{1}{2}a$ $CeO_2[110]$. In comparison with previously observed dislocation distances for this system (4.7[1] and 5.1 nm[27]), the dislocation network of the here presented films are in a significantly more relaxed state. A reason for the discrepancy between equilibrium spacing and the observed values could be the fact that the relaxed bulk lattices of the two materials form a Moire pattern (Figure 6(C)) with a the 45° rotated unit cell parameter of 6.5 nm (=18 CeO_2 or 19 YSZ 110 lattice planes). The observed dislocation network spacing could be the result of these two competing interface structures.

In the vicinity of the dislocations, the σ_{xx} strain map reveals tensile strain in the CeO_2 lattice and compressive strain in the YSZ lattice. The remaining σ_{yy}, σ_{xy}, and σ_{yx} strain tensor maps are presented in Figure S8(A–C), respectively. The σ_{yy} strain tensor map reveals a small, relatively homogeneous expansive strain in the CeO_2 film (Figure S8(A)) of ≈0.1%, well within the error bars of the GIXRD measurements. In addition, shear strain is also observed in the direct vicinity of the dislocation. Sign, amplitude, and location of the σ_{xy} and σ_{yx} components are nearly identical (Figure S8(B,C)) and in sum, correspond to a rotation of the interface lattice in the image plane in counter clockwise direction. Shear strain was observed both along and perpendicular to the interface normal (Figure S8(B,C)) with the same sign and value indicating a rotation of the lattice along the $[\bar{1}10]$ axis or along the image plane normal. In combination with the aforementioned rectangular holes appearing after the tube furnace annealing we deduct a complex relationship between out-of-plane strain, in-plane dislocation network, holes, and twisted CeO_2 lattice minimizing the interfacial energy between the two lattice mismatched materials. The recrystallization to larger domains observed by XRD and the increase in electron density observed by XRR indicate significant oxygen transfer through the bulk of the film from the environment. We suspect that the holes are condensated oxygen vacancies forming as the film restructuring from an oxygen deficient state (before the tube furnace annealing) to the fully oxidized state (after the tube furnace

https://doi.org/10.1021/acs.jpcc.4c04438
J. Phys. Chem. C 2024, 128, 19795−19806

annealing) occurs. In short, the restructuring to a perfect CeO_2 film is faster than oxygen can be supplied by the environment to the film. The rectangular footprint of the holes can be rationalized by the strong interaction of the surrounding film with the substrate and the significantly stronger oxygen diffusion across {100} planes compared to other directions.[53] In combination with the complex relaxation mechanism at the surface this results in a strong interaction between film and substrate at the interface which promotes the vacancy condensation to conform to the symmetry of the substrate and surrounding film leading to interruptions of the film at {100} and {010} planes resulting in rectangular holes.

Film Surface Composition. XPS measurements were conducted to analyze the chemical composition at the surface of the CeO_2 film after the tube furnace annealing. After introducing the sample to UHV, the sample was annealed at 450 °C with a backpressure of $5{\cdot}10^{-6}$ mbar O_2 to remove contaminative adsorbates. The survey scan in Figure S9 shows that the sample is free of contaminations. In Figure 7(A), the deconvoluted Ce 3d core level spectrum of the film is presented alongside reference spectra obtained from CeO_2 single crystal experiments (with linear background subtracted for comparability). The light gray curve represents an untreated Ce(111) single crystal, measured in normal emission, while the dark gray curve corresponds to a 111 faceted CeO_2(110) single crystal[54] measured in grazing incidence. For the latter, the authors reported a 35% Ce(III) content. The positions of 10 overlapping peaks of CeO_{2-x} are shown as black (Ce(IV)) and red (Ce(III)) dotted lines in Figure 7(A). For both cerium oxides $Ce^{IV}O_2$ and $Ce_2^{III}O_3$, only doublets are observed due to the $3d_{5/2}/3d_{3/2}$ spin−orbit splitting: One doublet for the primary photo emission (v/u for Ce(IV), v_0/u_0 for Ce(III)) process, two for shake-down processes in Ce(IV) (v''/u'', v'''/u''') and one for Ce(III) (v'/u').

Overall, the XPS data of the film closely resembles the bulk spectra of the CeO_2(111) single crystal (Figure 7(A), labeled (111) SC). Obvious contributions to the spectrum from Ce(III) (red dotted lines) like in the dark gray curve with 35% Ce(III) are clearly absent. Quantification of the amount of Ce(III) species is not trivial, especially for small amounts of Ce(III), as previously described in,[56−58] because of the large number of strongly overlapping, symmetric, and asymmetric peaks, combined with Shirley-background subtraction. Furthermore, extreme charging because of the large band gaps of CeO_2 and YSZ (3.0 and 4.23 eV respectively[59,60]) complicated the measurement. In order to simplify the fitting procedure we chose to restrict the fit by fixing doublet spacings to 18.4 eV, the doublet area ratio to 2/3, and the fwhm to the same value. An asymmetric peak profile composed of two Pseudo-Voigt profiles was chosen for the peaks v and u.[56,57,61] The spacing and fwhm between the asymmetry (indicated by blue arrows and corresponding position in Figure 7(A)) and the main components are equal for v and u. All components are Pseudo-Voigt line shapes with $\alpha = 0.8$ and the full set of fit parameters is given in Table S9. The resulting best fit of the described procedure is shown in red in Figure 7(A) and reproduces the data very well in all areas of the core level spectrum. No additional peaks were necessary at the expected positions of Ce(III) and including them resulted in worse agreement of fit and data, shift to Ce(IV) positions, fwhm of the order of 10 eV, or negligible peak areas, depending on the boundary conditions of the fit. In the same way, removing or reducing the asymmetry contribution to v and u did not yield improvement in the fit, independent of the inclusion or exclusion of Ce(III) components. From this, we conclude that within the error of measurement and fit, the surface of the CeO_2 film is fully oxidized. Further information on the oxidation state and surface chemistry of the film can be extracted from the O 1s and C 1s core levels shown in Figures 7(B) and S10, respectively. The two dominant components of the O 1s spectra are lattice oxygen at 529.0 eV[62,63] and water at 531.2 eV.[62,63] The spacing is in good agreement with previous studies on the surface of CeO_2(111) films supported by Pr_2O_3(0001)/Si(111) or metal substrates, and CeO_2 single crystals.[64,65] In order to fully reproduce the oxygen core level spectrum, an additional OH peak[66] and a carbon-related peak[67] were added at 530.16 and 532.73 eV, respectively. In agreement with the lack of Ce(III) signal in the Ce 3d core level spectra and the lack of a shoulder on the CeO_2 lattice oxygen peak, the addition of a lattice oxygen peak for partially reduced CeO_2 did not improve or maintain fit quality (full set of fit parameters in Table S10 and accompanying text). In order to understand the area distribution between the H_2O, OH, and lattice O peak, a layer analysis was conducted (detailed calculation is presented the Supporting Information (SI)) which revealed that the film is terminated by a 1.8 monolayer thick water film followed by one monolayer (0.95 ± 0.09) of OH. This clearly points toward a strongly hydroxylated surface which is further stabilized by the thin H_2O overlayer.

Polarization-resolved IRRAS was employed, using CO as a probe molecule, to gain further insight into the surface chemistry of the CeO_2 film. The CO surface ligand IR (CO-SLIR) approach[68] has been demonstrated to be well-suited for characterizing the surface structure of catalyst surfaces.[69−71] This is because the frequency of CO stretching vibrations is extremely sensitive to the chemical environment and varies significantly depending on the nature of adsorption sites. Figure 8(A) shows the corresponding p-polarized IRRAS data as a function of CO dosage at 65 K (cooling with liquid He). Upon CO adsorption on the cleaned CeO_2/YSZ thin film, no CO-related vibrational bands were observed in the region of

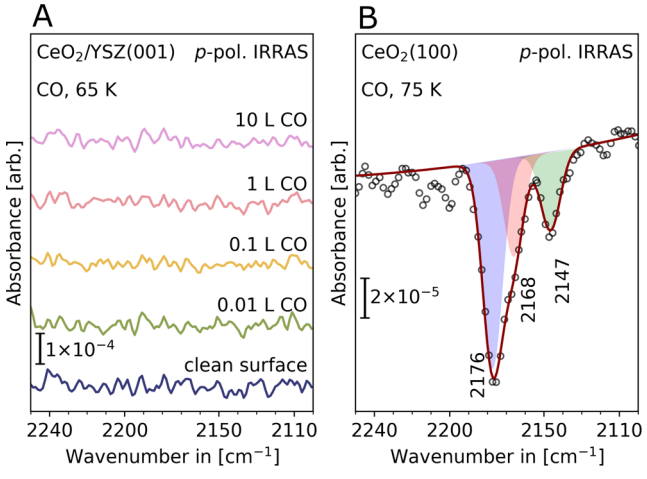

Figure 8. Surface structure of the oxidized CeO_2/YSZ(001) thin film characterized by polarization-resolved IRRAS. (A) p-polarized IRRAS data of CO adsorption at 65 K on CeO_2/YSZ(001). (B) Reference IRRA spectrum of CO adsorption on the (2 × 2) O-terminated CeO_2(100) single-crystal.[35]

https://doi.org/10.1021/acs.jpcc.4c04438
J. Phys. Chem. C 2024, 128, 19795−19806

2200−2100 cm^{-1} (the same is true for the *s*-polarized spectrum shown in Figure S11). For comparison, the IRRAS data of CO adsorption on the oxidized CeO_2(001) single crystal surface recorded at slightly higher temperatures (75 K) is presented in Figure 8(B). The bulk-truncated, polar CeO_2(001) surface is known to be inherently unstable, leading to its reconstruction into a (2 × 2) pattern for polarity compensation.[35] As shown in Figure 8(B), the charge neutral (2 × 2) O-terminated CeO_2(001) surface is characterized by two CO bands at 2147 and 2176 cm^{-1}, which are respectively assigned to CO species in an on-top and a bridge configuration, as supported by theoretical calculations using the hybrid density functional theory (DFT) approach with the HSE06 functional.[36] The shoulder resolved at 2168 cm^{-1} originates from CO bound to oxygen vacancy sites as a minority species.[35,36] We note that comprehensive IRRAS results were reported for CO adsorption on all three low-index ceria single-crystal surfaces (CeO_2(111), CeO_2(110), CeO_2(100)) in both oxidized and reduced forms.[34−37] These data reveal that the CO stretching band is highly facet-dependent and remarkably sensitive to the presence of O vacancies.[11,33−36] Furthermore, blue shifts of the CO vibrations relative to the gas phase (2143 cm^{-1}) were observed for CO adsorption on all oxidized and reduced CeO_2 surfaces. Overall, the present IRRAS results provide solid evidence that the surface structure of the CeO_2(100) thin film is rather different from that observed for CeO_2(100) single-crystal surfaces. The absence of any CO-related IR signals, even at temperature as low as 65 K, suggests that the surface of the CeO_2(100) thin film is stabilized by hydroxylation, where the polar instability is removed through the formation of hydroxyl groups, in line with XPS observations.

CONCLUSIONS

We present a facile, stream-lined UHV growth procedure for epitaxial, fully oxidized CeO_2(100) thin films supported by YSZ(001) and report on their crystallographic, chemical, and morphological properties. With the presented growth procedure we were able to reduce the number of preparation steps compared to other studies using YSZ supports.[1,27] The films exhibit a fully coherent lattice along their surface normal over the full film thicknesses of 10 to 15 nm. The lattice is almost fully relaxed to the bulk lattice parameter, with a small tensile out-of-plane strain of ≈0.1%. The in-plane lattice of the film is fully relaxed via the formation of a long-range ordered dislocation network along the [110] directions. After the tube furnace annealing, the film is completely oxidized at both interfaces and in the bulk, as no reduced electron density was observed in XRR and no significant Ce(III) population could be observed by XPS. The prepared films exhibit rectangular holes with edges aligned with the [100] and [010] axes. These holes are local phenomena and a result of the restructuring process occurring during the tube furnace annealing. Spectroscopic analysis by IRRAS and XPS as well as structural investigation by CTR analysis show that the point defect free surface is hydroxylated and (001) terminated. Similar to reports on ZrO_2, the surface is found to be fully hydroxylated for charge compensation of the polar (001) surface of CeO_2,[72,73] demonstrating its high activity toward water dissociation, occurring likely during the tube furnace annealing process.[74] The films represent an ideal support for the preparation of model heterogeneous catalysts by metal nanoparticle deposition for elucidating structure−activity relationships.

ASSOCIATED CONTENT

Supporting Information

The Supporting Information is available free of charge at https://pubs.acs.org/doi/10.1021/acs.jpcc.4c04438.

Additional SEM, AES, AFM, GIXRD, HR-STEM, and geometric phase analysis data, models used for fitting, and fit parameters (PDF)

AUTHOR INFORMATION

Corresponding Authors

Jan-Christian Schober − *Centre for X-ray and Nano Science, Deutsches Elektronen-Synchrotron DESY, 22607 Hamburg, Germany; Universität Hamburg, 20148 Hamburg, Germany;* orcid.org/0000-0002-4084-123X; Email: jan-christian.schober@desy.de

Andreas Stierle − *Centre for X-ray and Nano Science, Deutsches Elektronen-Synchrotron DESY, 22607 Hamburg, Germany; Universität Hamburg, 20148 Hamburg, Germany;* orcid.org/0000-0002-0303-6282; Email: andreas.stierle@desy.de

Authors

E. Erik Beck − *Centre for X-ray and Nano Science, Deutsches Elektronen-Synchrotron DESY, 22607 Hamburg, Germany; Universität Hamburg, 20148 Hamburg, Germany;* orcid.org/0000-0001-6284-5269

Ming-Chao Kao − *Centre for X-ray and Nano Science, Deutsches Elektronen-Synchrotron DESY, 22607 Hamburg, Germany; Universität Hamburg, 20148 Hamburg, Germany;* orcid.org/0000-0002-6443-214X

Mona Kohantorabi − *Centre for X-ray and Nano Science, Deutsches Elektronen-Synchrotron DESY, 22607 Hamburg, Germany;* orcid.org/0000-0002-4230-8797

Marcus Creutzburg − *Centre for X-ray and Nano Science, Deutsches Elektronen-Synchrotron DESY, 22607 Hamburg, Germany;* orcid.org/0000-0002-3639-6049

Dmitri V. Novikov − *Deutsches Elektronen-Synchrotron DESY, 22607 Hamburg, Germany*

Thomas F. Keller − *Centre for X-ray and Nano Science, Deutsches Elektronen-Synchrotron DESY, 22607 Hamburg, Germany; Universität Hamburg, 20148 Hamburg, Germany;* orcid.org/0000-0002-3770-6344

Birger Holtermann − *Laboratory for Electron Microscopy (LEM), Karlsruhe Institute of Technology KIT, 76131 Karlsruhe, Germany*

Nadejda Firman − *Laboratory for Electron Microscopy (LEM), Karlsruhe Institute of Technology KIT, 76131 Karlsruhe, Germany*

Lachlan Caulfield − *Institute of Functional Interfaces (IFG), Karlsruhe Institute of Technology KIT, 76344 Karlsruhe, Germany*

Eric Sauter − *Institute of Functional Interfaces (IFG), Karlsruhe Institute of Technology KIT, 76344 Karlsruhe, Germany*

Vedran Vonk − *Centre for X-ray and Nano Science, Deutsches Elektronen-Synchrotron DESY, 22607 Hamburg, Germany;* orcid.org/0000-0001-9854-1101

Christof Wöll − *Institute of Functional Interfaces (IFG), Karlsruhe Institute of Technology KIT, 76344 Karlsruhe, Germany;* orcid.org/0000-0003-1078-3304
Yuemin Wang − *Institute of Functional Interfaces (IFG), Karlsruhe Institute of Technology KIT, 76344 Karlsruhe, Germany;* orcid.org/0000-0002-9963-5473
Heshmat Noei − *Centre for X-ray and Nano Science, Deutsches Elektronen-Synchrotron DESY, 22607 Hamburg, Germany;* orcid.org/0000-0003-1294-3527
Yolita M. Eggeler − *Laboratory for Electron Microscopy (LEM), Karlsruhe Institute of Technology KIT, 76131 Karlsruhe, Germany*

Complete contact information is available at: https://pubs.acs.org/10.1021/acs.jpcc.4c04438

Notes

The authors declare no competing financial interest.

■ ACKNOWLEDGMENTS

This work was supported by the Deutsche Forschungsgemeinschaft, Germany (DFG, German Research Foundation) via SFB 1441, Project-ID 426888090. We acknowledge DESY (Hamburg, Germany), a member of the Helmholtz Association HGF, for the provision of experimental facilities. Parts of this research were carried out at PETRA III and we would like to thank Dmitri Novikov for assistance in using P23 "In situ X-ray diffraction and imaging". Beamtime was allocated for proposal I-20211656."We further would like to acknowledge the work of Dennis Renner and Simon Geile for technical support in the UHV- and X-ray laboratories.

■ REFERENCES

(1) Wang, C.-M.; Thevuthasan, S.; Peden, C. H. F. Interface Structure of an Epitaxial Cubic Ceria Film on Cubic Zirconia. *J. Am. Ceram. Soc.* **2003**, *86*, 363−365.
(2) Barth, C.; Laffon, C.; Olbrich, R.; Ranguis, A.; Parent, P.; Reichling, M. A Perfectly Stoichiometric and Flat CeO_2(111) Surface on a Bulk-Like Ceria Film. *Sci. Rep.* **2016**, *6*, No. 21165.
(3) Wu, F.; Pavlovska, A.; Smith, D. J.; Culbertson, R. J.; Wilkens, B. J.; Bauer, E. Growth and Structure of Epitaxial CeO_2 Films on Yttria-Stabilized ZrO_2. *Thin Solid Films* **2008**, *516*, 4908−4914.
(4) Bozo, C.; Guilhaume, N.; Herrmann, J.-M. Role of the Ceria-Zirconia Support in the Reactivity of Platinum and Palladium Catalysts for Methane Total Oxidation under Lean Conditions. *J. Catal.* **2001**, *203*, 393−406.
(5) Montini, T.; Melchionna, M.; Monai, M.; Fornasiero, P. Fundamentals and Catalytic Applications of CeO_2-Based Materials. *Chem. Rev.* **2016**, *116*, 5987−6041.
(6) Mi, R.; Li, D.; Hu, Z.; Yang, R. T. Morphology Effects of CeO_2 Nanomaterials on the Catalytic Combustion of Toluene: A Combined Kinetics and Diffuse Reflectance Infrared Fourier Transform Spectroscopy Study. *ACS Catal.* **2021**, *11*, 7876−7889.
(7) Guo, Y.; Qin, Y.; Liu, H.; Wang, H.; Han, J.; Zhu, X.; Ge, Q. CeO_2 Facet-Dependent Surface Reactive Intermediates and Activity during Ketonization of Propionic Acid. *ACS Catal.* **2022**, *12*, 2998−3012.
(8) Spezzati, G.; Benavidez, A. D.; DeLaRiva, A. T.; et al. CO Oxidation by Pd Supported on CeO_2(100) and CeO_2(111) Facets. *Appl. Catal., B* **2019**, *243*, 36−46.
(9) Colussi, S.; Fornasiero, P.; Trovarelli, A. Structure-Activity Relationship in Pd/CeO_2 Methane Oxidation Catalysts. *Chin. J. Catal.* **2020**, *41*, 938−950.
(10) Liu, J.-X.; Su, Y.; Filot, I. A. W.; Hensen, E. J. M. A Linear Scaling Relation for CO Oxidation on CeO_2-Supported Pd. *J. Am. Chem. Soc.* **2018**, *140*, 4580−4587.
(11) Maurer, F.; Jelic, J.; Wang, J.; Gänzler, A.; Dolcet, P.; Wöll, C.; Wang, Y.; Studt, F.; Casapu, M.; Grunwaldt, J.-D. Tracking the Formation, Fate and Consequence for Catalytic Activity of Pt Single Sites on CeO_2. *Nat. Catal.* **2020**, *3*, 824−833.
(12) Song, B.; Si, S.; Soleymani, A.; Xin, Y.; Hagelin-Weaver, H. E. Effect of Ceria Surface Facet on Stability and Reactivity of Isolated Platinum Atoms. *Nano Res.* **2022**, *15*, 5922−5932.
(13) Costa-Nunes, O.; Gorte, R. J.; Vohs, J. M. High Mobility of Ceria Films on Zirconia at Moderate Temperatures. *J. Mater. Chem.* **2005**, *15*, 1520−1522.
(14) Dolcet, P.; Maurer, F.; Casapu, M.; Grunwaldt, J.-D. Insights into the Structural Dynamics of Pt/CeO_2 Single-Site Catalysts during CO Oxidation. *Catalysts* **2021**, *11*, No. 617.
(15) Yang, C.; Cao, Y.; Plessow, P. N.; et al. N_2O Adsorption and Photochemistry on Ceria Surfaces. *J. Phys. Chem. C* **2022**, *126*, 2253−2263.
(16) Maurer, F.; Beck, A.; Jelic, J.; et al. Surface Noble Metal Concentration on Ceria as a Key Descriptor for Efficient Catalytic CO Oxidation. *ACS Catal.* **2022**, *12*, 2473−2486.
(17) Maurer, F.; Gänzler, A.; Lott, P.; et al. Spatiotemporal Investigation of the Temperature and Structure of a Pt/CeO_2 Oxidation Catalyst for CO and Hydrocarbon Oxidation during Pulse Activation. *Ind. Eng. Chem. Res.* **2021**, *60*, 6662−6675.
(18) Sauerbrey, M.; Gasperi, G.; Luches, P.; Falta, J.; Valeri, S.; Flege, J. I. Cerium Oxide Epitaxial Nanostructures on Pt(111): Growth, Morphology and Structure. *Top. Catal.* **2017**, *60*, 513−521.
(19) Hasegawa, T.; Shahed, S. M. F.; Sainoo, Y.; Beniya, A.; Isomura, N.; Watanabe, Y.; Komeda, T. Epitaxial Growth of CeO_2(111) Film on Ru(0 0 0 1): Scanning Tunneling Microscopy (STM) and X-ray Photoemission Spectroscopy (XPS) Study. *J. Chem. Phys.* **2014**, *140*, No. 044711.
(20) Pieper, H. H.; Derks, C.; Zoellner, M. H.; Olbrich, R.; Tröger, L.; Schroeder, T.; Neumann, M.; Reichling, M. Morphology and Nanostructure of CeO_2(111) Surfaces of Single Crystals and Si(111) Supported Ceria Films. *Phys. Chem. Chem. Phys.* **2012**, *14*, 15361−15368.
(21) Olbrich, R.; Pieper, H. H.; Oelke, R.; Wilkens, H.; Wollschläger, J.; Zoellner, M. H.; Schroeder, T.; Reichling, M. A Well-Structured Metastable Ceria Surface. *Appl. Phys. Lett.* **2014**, *104*, No. 081910.
(22) Nandasiri, M. I.; Nachimuthu, P.; Varga, T.; Shutthanandan, V.; Jiang, W.; Kuchibhatla, S. V. N. T.; Thevuthasan, S.; Seal, S.; Kayani, A. Influence of Growth Rate on the Epitaxial Orientation and Crystalline Quality of CeO_2 Thin Films Grown on Al_2O_3(0 0 0 1). *J. Appl. Phys.* **2011**, *109*, No. 013525.
(23) Kaemena, B.; Senanayake, S. D.; Meyer, A.; Sadowski, J. T.; Falta, J.; Flege, J. I. Growth and Morphology of Ceria on Ruthenium(0001). *J. Phys. Chem. C* **2013**, *117*, 221−232.
(24) Mullins, D. R.; Radulovic, P. V.; Overbury, S. H. Ordered Cerium Oxide Thin Films Grown on Ru(0001) and Ni(111). *Surf. Sci.* **1999**, *429*, 186−198.
(25) Luches, P.; Pagliuca, F.; Valeri, S. Morphology, Stoichiometry, and Interface Structure of CeO_2 Ultrathin Films on Pt(111). *J. Phys. Chem. C* **2011**, *115*, 10718−10726.
(26) Zscherp, M. F.; Glaser, J.; Becker, C.; Beyer, A.; Cop, P.; Schörmann, J.; Volz, K.; Elm, M. T. Epitaxial Growth and Structural Characterization of Ceria Deposited by Atomic Layer Deposition on High-Surface Porous Yttria-Stabilized Zirconia Thin Films. *Cryst. Growth Des.* **2020**, *20*, 2194−2201.
(27) Shi, Y.; Lee, S. C.; Monti, M.; Wang, C.; Feng, Z. A.; Nix, W. D.; Toney, M. F.; Sinclair, R.; Chueh, W. C. Growth of Highly Strained CeO_2 Ultrathin Films. *ACS Nano* **2016**, *10*, 9938−9947.
(28) Niu, G.; Zoellner, M. H.; Schroeder, T.; et al. Controlling the Physics and Chemistry of Binary and Ternary Praseodymium and Cerium Oxide Systems. *Phys. Chem. Chem. Phys.* **2015**, *17*, 24513−24540.
(29) Torbrügge, S.; Reichling, M.; Ishiyama, A.; Morita, S.; Custance, O. Evidence of Subsurface Oxygen Vacancy Ordering on Reduced CeO_2(111). *Phys. Rev. Lett.* **2007**, *99*, No. 056101.

(30) Su, Z.; Yang, W.; Wang, C.; Xiong, S.; Cao, X.; Peng, Y.; Si, W.; Weng, Y.; Xue, M.; Li, J. Roles of Oxygen Vacancies in the Bulk and Surface of CeO_2 for Toluene Catalytic Combustion. *Environ. Sci. Technol.* **2020**, *54*, 12684−12692.
(31) Li, Z.; Werner, K.; Chen, L.; et al. Interaction of Hydrogen with Ceria: Hydroxylation, Reduction, and Hydride Formation on the Surface and in the Bulk. *Chem. - Eur. J.* **2021**, *27*, 5268−5276.
(32) Wu, X.-P.; Gong, X.-Q. Clustering of Oxygen Vacancies at CeO_2(111): Critical Role of Hydroxyls. *Phys. Rev. Lett.* **2016**, *116* (8), No. 086102.
(33) Caulfield, L.; Sauter, E.; Idriss, H.; Wang, Y.; Wöll, C. Bridging the Pressure and Materials Gap in Heterogeneous Catalysis: A Combined UHV, In Situ, and Operando Study Using Infrared Spectroscopy. *J. Phys. Chem. C* **2023**, *127*, 14023−14029.
(34) Yang, C.; Yu, X.; Heißler, S.; Nefedov, A.; Colussi, S.; Llorca, J.; Trovarelli, A.; Wang, Y.; Wöll, C. Surface Faceting and Reconstruction of Ceria Nanoparticles. *Angew. Chem., Int. Ed.* **2017**, *56*, 375−379.
(35) Yang, C.; Capdevila-Cortada, M.; Dong, C.; et al. Surface Refaceting Mechanism on Cubic Ceria. *J. Phys. Chem. Lett.* **2020**, *11*, 7925−7931.
(36) Lustemberg, P. G.; Yang, C.; Wang, Y.; Wöll, C.; Ganduglia-Pirovano, M. V. Vibrational Frequencies of CO Bound to All Three Low-Index Cerium Oxide Surfaces: A Consistent Theoretical Description of Vacancy-Induced Changes Using Density Functional Theory. *J. Chem. Phys.* **2023**, *159*, No. 034704.
(37) Lustemberg, P. G.; Plessow, P. N.; Wang, Y.; Yang, C.; Nefedov, A.; Studt, F.; Wöll, C.; Ganduglia-Pirovano, M. V. Vibrational Frequencies of Cerium-Oxide-Bound CO: A Challenge for Conventional DFT Methods. *Phys. Rev. Lett.* **2020**, *125*, No. 256101.
(38) Esch, F.; Fabris, S.; Zhou, L.; Montini, T.; Africh, C.; Fornasiero, P.; Comelli, G.; Rosei, R. Electron Localization Determines Defect Formation on Ceria Substrates. *Science* **2005**, *309*, 749−752.
(39) Kullgren, J.; Wolf, M. J.; Castleton, C. W. M.; Mitev, P.; Briels, W. J.; Hermansson, K. Oxygen Vacancies versus Fluorine at CeO_2(111): A Case of Mistaken Identity? *Phys. Rev. Lett.* **2014**, *112*, No. 156102.
(40) Stierle, A.; Keller, T.; Noei, H.; Vonk, V.; Roehlsberger, R. DESY NanoLab. *J. Large-Scale Res. Facil., JLSRF* **2016**, *2*, No. A76.
(41) Nečas, D.; Klapetek, P. Gwyddion An Open-Source Software for SPM Data Analysis. *Cent. Eur. J. Phys.* **2012**, *10*, 181−188.
(42) Kriegner, D.; Wintersberger, E. xrayutilities, 2023. https://xrayutilities.sourceforge.io/index.html. last visited November 06, 2023.
(43) Parratt, L. G. Surface Studies of Solids by Total Reflection of X-rays. *Phys. Rev.* **1954**, *95*, No. 359.
(44) Arndt, B.; Noei, H.; Keller, T. F.; Müller, P.; Vonk, V.; Nenning, A.; Opitz, A. K.; Fleig, J.; Rütt, U.; Stierle, A. Structure and Stability of Gd-Doped CeO_2 Thin Films on Yttria-Stabilized Zirconia. *Thin Solid Films* **2016**, *603*, 56−61.
(45) Debye, P.; Scherrer, P. Bestimmung der Größe und der Inneren Struktur von Kolloidteilchen Mittels Röntgenstrahlen. In *Nachrichten von der Gesellschaft der Wissenschaften zu Göttingen, Mathematisch-Physikalische Klasse*; Forgotten Books, 1918; Vol. *1*, pp 98−100.
(46) Ma, Y.; Ma, Y.; Giuli, G.; et al. Introducing Highly Redox-Active Atomic Centers into Insertion-Type Electrodes for Lithium-Ion Batteries. *Adv. Energy Mater.* **2020**, *10*, No. 2000783.
(47) Stierle, A.; Vlieg, E. *Modern Diffraction Methods*; John Wiley & Sons, Ltd., 2012; Chapter 8, pp 221−257.
(48) Robinson, I. K. Crystal Truncation Rods and Surface Roughness. *Phys. Rev. B* **1986**, *33*, No. 3830.
(49) Renbaud, G.; Guenard, P.; Barbier, A. Misfit Dislocation Network at the Ag/MgO(0 0 1) Interface: A Grazing Incidence X-ray-Scattering Study. *Phys. Rev. B* **1998**, *58*, No. 7310.
(50) Wintersberger, E.; Hrauda, N.; Kriegner, D.; et al. Analysis of Periodic Dislocation Networks using X-ray Diffraction and Extended Finite Element Modeling. *Appl. Phys. Lett.* **2010**, *96*, No. 131905.
(51) Hytch, M. Geometric Phase Analysis of High Resolution Electron Microscope Images. *Scanning Microsc.* **1997**, *11*, 53−66.
(52) Kim, K.-H. Digital Micrograph Script Source Listing for a Geometric Phase Analysis. *Appl. Microsc.* **2015**, *45*, 101−105.
(53) Zhu, L.; Jin, X.; Zhang, Y. Y.; et al. Visualizing Anisotropic Oxygen Diffusion in Ceria under Activated Conditions. *Phys. Rev. Lett.* **2020**, *124*, No. 056002.
(54) Yang, C.; Yu, X.; Heißler, S.; Nefedov, A.; Colussi, S.; Llorca, J.; Trovarelli, A.; Wang, Y.; Wöll, C. Surface Faceting and Reconstruction of Ceria Nanoparticles. *Angew. Chem., Int. Ed.* **2017**, *56*, 375−379.
(55) Li, Z.; Werner, K.; Qian, K.; et al. Oxidation of Reduced Ceria by Incorporation of Hydrogen. *Angew. Chem., Int. Ed.* **2019**, *58*, 14686−14693.
(56) Świątowska, J.; Lair, V.; Pereira-Nabais, C.; Cote, G.; Marcus, P.; Chagnes, A. XPS, XRD and SEM Characterization of a Thin Ceria Layer Deposited onto Graphite Electrode for Application in Lithium-Ion Batteries. *Appl. Surf. Sci.* **2011**, *257*, 9110−9119.
(57) Skála, T.; Šutara, F.; Prince, K. C.; Matolín, V. Cerium Oxide Stoichiometry Alteration via Sn Deposition: Influence of Temperature. *J. Electron Spectrosc. Relat. Phenom.* **2009**, *169*, 20−25.
(58) Alammar, T.; Noei, H.; Wang, Y.; Grünert, W.; Mudring, A.-V. Ionic Liquid-Assisted Sonochemical Preparation of CeO_2 Nanoparticles for CO Oxidation. *ACS Sustainable Chem. Eng.* **2015**, *3*, 42−54.
(59) Kusmierek, E. A. CeO_2 Semiconductor as a Photocatalytic and Photoelectrocatalytic Material for the Remediation of Pollutants in Industrial Wastewater: A Review. *Catalysts* **2020**, *10*, No. 1435.
(60) PaiVerneker, V. R.; Petelin, A. N.; Crowne, F. J.; Nagle, D. C. Color-Center-Induced Band-Gap Shift in Yttria-Stabilized Zirconia. *Phys. Rev. B* **1989**, *40*, No. 8555.
(61) Engelhard, M.; Azad, S.; Peden, C.; Thevuthasan, S. X-ray Photoelectron Spectroscopy Studies of Oxidized and Reduced CeO_2(111) Surfaces. *Surf. Sci. Spectra* **2004**, *11*, 73−81.
(62) Lykhach, Y.; Johánek, V.; Aleksandrov, H. A.; et al. Water Chemistry on Model Ceria and Pt/Ceria Catalysts. *J. Phys. Chem. C* **2012**, *116*, 12103−12113.
(63) Fu, S.-P.; Rossero, J.; Chen, C.; Li, D.; Takoudis, C. G.; Abiade, J. T. On the wetting behavior of ceria thin films grown by pulsed laser deposition. *Appl. Phys. Lett.* **2017**, *110*, No. 081601.
(64) Mullins, D.; Overbury, S.; Huntley, D. Electron Spectroscopy of Single Crystal and Polycrystalline Cerium Oxide Surfaces. *Surf. Sci.* **1998**, *409*, 307−319.
(65) Kundakovic, L.; Mullins, D.; Overbury, S. Adsorption and Reaction of H_2O and CO on Oxidized and Reduced Rh/CeO_x(111) Surfaces. *Surf. Sci.* **2000**, *457*, 51−62.
(66) Chanu, W. C.; Gupta, A.; Singh, M. K.; Pandey, O. P. Group V Elements (V, Nb and Ta) Doped CeO_2 Particles for Efficient Photo-Oxidation of Methylene Blue Dye. *J. Inorg. Organomet. Polym. Mater.* **2021**, *31*, 636−647.
(67) Min, C.; He, Z.; Song, H.; Liu, D.; Jia, W.; Qian, J.; Jin, Y.; Guo, L. Fabrication of Novel CeO_2/GO/CNTs Ternary Nanocomposites with Enhanced Tribological Performance. *Appl. Sci.* **2019**, *9*, No. 170.
(68) Wöll, C. Structure and Chemical Properties of Oxide Nanoparticles Determined by Surface-Ligand IR Spectroscopy. *ACS Catal.* **2020**, *10*, 168−176.
(69) Wang, J.; Sauter, E.; Nefedov, A.; Heißler, S.; Maurer, F.; Casapu, M.; Grunwaldt, J.-D.; Wang, Y.; Wöll, C. Dynamic Structural Evolution of Ceria-Supported Pt Particles: A Thorough Spectroscopic Study. *J. Phys. Chem. C* **2022**, *126*, 9051−9058.
(70) Chen, A.; Yu, X.; Zhou, Y.; et al. Structure of the Catalytically Active Copper-Ceria Interfacial Perimeter. *Nat. Catal.* **2019**, *2*, 334−341.
(71) Liu, S.; Li, Y.; Yu, X.; et al. Tuning Crystal-Phase of Bimetallic Single-Nanoparticle for Catalytic Hydrogenation. *Nat. Commun.* **2022**, *13*, No. 4559.
(72) Iskandarova, I.; Knizhnik, A.; Rykova, E.; Bagatur'yants, A.; Potapkin, B.; Korkin, A. First-Principle Investigation of the

Hydroxylation of Zirconia and Hafnia Surfaces. *Microelectron. Eng.* **2003**, *69*, 587−593.
(73) Köck, E.-M.; Kogler, M.; Bielz, T.; Klötzer, B.; Penner, S. In Situ FT-IR Spectroscopic Study of CO_2 and CO Adsorption on Y_2O_3, ZrO_2, and Yttria-Stabilized ZrO_2. *J. Phys. Chem. C* **2013**, *117*, 17666−17673.
(74) Chen, S.; Pleßow, P. N.; Yu, Z.; Sauter, E.; Caulfield, L.; Nefedov, A.; Studt, F.; Wang, Y.; Wöll, C. Structure and Chemical Reactivity of Y-Stabilized ZrO_2 Surfaces: Importance for the Water-Gas Shift Reaction. *Angew. Chem., Int. Ed.* **2024**, *63*, No. e202404775.

https://doi.org/10.1021/acs.jpcc.4c04438
J. Phys. Chem. C 2024, 128, 19795−19806